ACS NANO

www.acsnano.org

ARTICLE

# Unraveling the Emission Pathways in Copper Indium Sulfide Quantum Dots

Chenghui Xia, Philippe Tamarat, Lei Hou, Serena Busatto, Johannes D. Meeldijk, Celso de Mello Donega, and Brahim Lounis*

Cite This: *ACS Nano* 2021, 15, 17573−17581

Read Online

ACCESS | Metrics & More | Article Recommendations | Supporting Information

**ABSTRACT:** **Semiconductor copper indium sulfide quantum dots are emerging as promising alternatives to cadmium- and lead-based chalcogenides in solar cells, luminescent solar concentrators, and deep-tissue bioimaging due to their inherently lower toxicity and outstanding photoluminescence properties. However, the nature of their emission pathways remains a subject of debate. Using low-temperature single quantum dot spectroscopy on core−shell copper indium sulfide nanocrystals, we observe two subpopulations of particles with distinct spectral features. The first class shows sharp resolution-limited emission lines that are attributed to zero-phonon recombination lines of a long-lived band-edge exciton. Such emission results from the perfect passivation of the copper indium sulfide core by the zinc sulfide shell and points to an inversion in the band-edge hole levels. The second class exhibits ultrabroad spectra regardless of the temperature, which is a signature of the extrinsic self-trapping of the hole assisted by defects in imperfectly passivated quantum dots.**

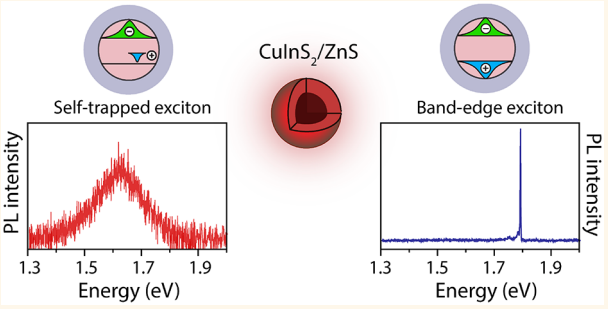


**KEYWORDS:** *core−shell nanocrystals, single dot spectroscopy, exciton, fine structure, exciton−phonon coupling, exciton self-trapping*

Colloidal semiconductor copper indium sulfide (CIS) quantum dots (QDs) are promising alternatives to Cd- and Pb-based nanocrystals due to their inherently lower toxicity, large absorption cross section over a broad spectral range, long radiative lifetime (viz. tens to hundreds of nanoseconds), and large Stokes shifts (~300−500 meV) with a wide photoluminescence (PL) tunability from the visible to the second near-infrared biological window.[1−5] These properties make them particularly attractive for QD-sensitized solar cells,[6] luminescent solar concentrators,[7,8] and bioimaging.[9,10] Bare CIS QDs usually show low PL quantum yields and a poor photostability, thus restricting their direct use for applications.[1−5] These limitations can be circumvented by overcoating them with a shell of wide bandgap semiconductors (e.g., ZnS and CdS).[10,11] With the advanced development of colloidal synthesis and postshelling procedures, the state-of-the-art CIS-based core−shell QDs exhibit low size dispersion, excellent photostability, and competing PL quantum yields over 80%.[8,11,12] Strikingly, their absorption and emission bandwidths (~200−400 meV) are much larger than those of the prototypical binary QDs[13−15] regardless of their size and shape dispersions or their compositions. After more than a decade of extensive experimental and theoretical work, the emission from these nanostructures is considered to stem from the recombination of a delocalized conduction band (CB) electron with a localized hole.[1,2,11,12,16−23] Yet, the nature of the hole localization site has still not been elucidated. The hole may be captured by either a $Cu^+$-related defect[18,22,24] or self-trapping,[16,19,20] leading to an ongoing debate on the origin of the PL broadening in CIS QDs. Moreover, unlike their bulk counterparts,[25] the emission from the band-edge exciton has never been reported in CIS QDs. Thus, the theoretical model developed to explain the large Stokes shifts and long radiative lifetimes with a band-edge hole-level inversion[26] has not been confronted to any luminescence spectroscopy result.

Single-dot spectroscopy is the method of choice to unravel the nature of the physical mechanisms at the origin of the PL in CIS-based QDs. In early spectroscopic studies, the room-temperature PL line width (~200 meV) of single CIS/CdS QDs was found to be slightly narrower than that of QD ensembles[17] and was interpreted as the manifestation of strong electron−phonon coupling induced by hole self-trapping on

Received: June 9, 2021
Accepted: September 20, 2021
Published: September 21, 2021

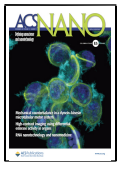









https://doi.org/10.1021/acsnano.1c04909
*ACS Nano* 2021, 15, 17573−17581

regular $Cu^+$ sites.[16] Later, single CIS/ZnS QD PL line widths as narrow as ~60 meV,[18] which are comparable to those of single CdSe QDs,[13,14] were reported and considered as the signature of the recombination of a delocalized CB electron with a hole localized on a Cu-related defect. Therefore, the broad ensemble PL spectra have been attributed to random positioning of the emissive centers within the QDs.[18] Those studies thus lead to contradictory results and disparate interpretations regarding the origin of the PL line width broadening and the nature of the hole-localizing center, while knowledge of the fundamental optical properties of CIS QDs is essential for the design of CIS QD-based light emitting and optoelectronic devices.

Here, we perform low-temperature spectroscopy of single CIS/ZnS QDs to unravel the photophysical properties and ultimate PL line widths of these nanostructures. Two subpopulations of QDs were identified, the first displaying emission lines nearly as broad as those at room temperature and the second exhibiting sharp resolution-limited zero-phonon lines (ZPL) at liquid helium temperature. Our spectroscopic measurements let us infer that the broad spectra originate from defect-assisted exciton self-trapping, while the sharp ZPLs stem from radiative recombination of the band-edge exciton. Single-QD PL decays and magneto-optical spectra of the band-edge exciton give insights into the fine structure and relaxation dynamics and shed light on the symmetry of the upper hole levels. These findings will guide the development of accurate theoretical models of exciton states and emission pathways in CIS-based QDs in the view of potential optoelectronic applications.

## RESULTS AND DISCUSSION

The CIS/ZnS QDs used in these studies were prepared from wurtzite (wz) CIS cores grown by topotactic partial $Cu^+$-for-$In^{3+}$ cation exchange in template $Cu_{2-x}S$ nanocrystals, which were then heteroepitaxially capped with a ZnS shell. Figure 1a shows that the nanoparticles are composed of nearly stochiometric CIS cores (Cu/In ~ 1) capped with a thick shell of ZnS (Figure 1b). The average QD size is 7.4 ± 0.6 nm (Figure 1a), while that of the cores is (4.9 ± 0.4 nm) (Supporting Information, SI Figure S1), indicating that around four monolayers of ZnS were grown on the CIS core. The small particles are pure ZnS that nucleated during the shelling procedure (SI Figure S2). Selected-area electron diffraction analysis (Figure 1c) together with high-resolution TEM images (Figure 1d and SI Figure S3) clearly show that the CIS/ZnS QDs keep a hexagonal wz crystal structure after the ZnS shelling. Compared with chalcopyrite (cp) CIS/ZnS QDs,[27] these QDs have narrower size and shape distributions and a redshifted emission due to their smaller CIS bandgap. Their near-infrared emission range is thus relevant for various applications, such as luminescent solar concentrators or in vivo bioimaging.

The room-temperature absorption and PL spectra of the bare CIS cores and CIS/ZnS QDs are presented in Figure 2a. The wz-CIS cores exhibit a broad PL line width and a featureless absorption transition with a low-energy absorption tail that extends far below the bulk CIS bandgap (~1.3 eV).[28,29] The tail is also commonly observed in chalcopyrite CIS QDs[1−5] and can be attributed to Cu-related sub-bandgap state absorption.[1−5,16,23,30] After capping the CIS core with ZnS, the overall PL quantum yield significantly improved to 55 ± 5% and a slight blue shift by ~40 meV was observed in the

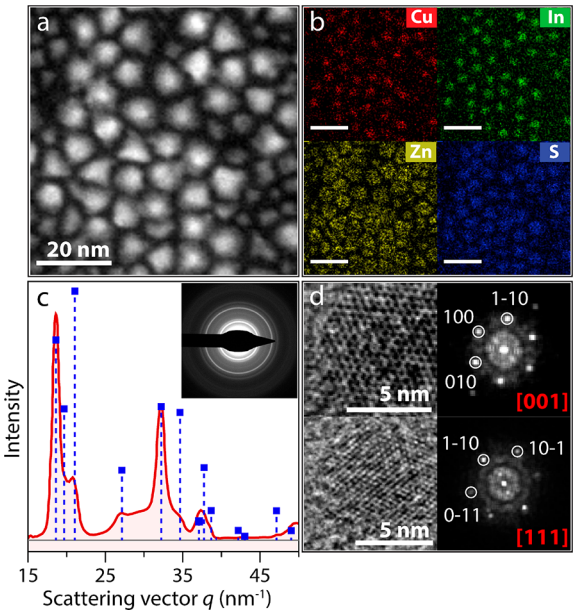


**Figure 1. Characterization of the CIS/ZnS core−shell nanocrystals. (a) High-angle annular dark field-scanning transmission electron microscopy image of the product CIS/ZnS QDs. (b) Corresponding elemental maps with scale bars of 20 nm. (c) One-dimensional electron diffraction pattern obtained by the azimuthal integration of the two-dimensional electron diffraction pattern shown in the inset. The diffraction peaks are in accordance with those of wz-CIS (PDF no. 01-077-9459). (d) High-resolution TEM images (left column) and corresponding Fourier transform patterns (right column) of two CIS/ZnS QDs. The Fourier transform patterns are indexed to the axial projection of the hexagonal wz-CIS structure along the [001] and [111] directions from top to bottom, respectively. See the Methods section for details of the QD synthesis, the sample preparation, and characterization.**

absorption spectrum, indicating an increase in the band-edge exciton energy. This can be ascribed to partial $Zn^{2+}$-for-$In^{3+}$ and $Cu^+$ cation exchange followed by interdiffusion, which leads to an increase of the core semiconductor bandgap.[12,31] Another possibility is that the core diameter shrinks due to either etching prior to the shell overgrowth[11,32] or shell ingrowth by cation exchange,[18,33] resulting in a stronger quantum confinement of the charge carriers. Moreover, the lattice compression of the CIS cores by the thick ZnS shell leads to strain that may further shift the exciton energy levels to higher energies, as was also observed in prototypical CdSe/CdS QDs.[34] The low-energy absorption tail is significantly reduced in the CIS/ZnS core−shell QDs (Figure 2a), implying that the ZnS shell suppresses sub-bandgap state absorption by stoichiometry or surface chemistry modifications in the cores. Strikingly, the PL spectrum of CIS/ZnS QDs exhibits a global blue shift by more than 240 meV with respect to that of the CIS cores, i.e., five times larger than the blue shift observed in the absorption spectrum (Figure 2a). This shift can be attributed to an efficient passivation of surface traps or inner defects that induce deep intrabandgap states.[35,36]

Interestingly, two sub-bands show up in the PL spectra of CIS/ZnS QDs in solution (Figure 2a) or those embedded in a poly(methyl methacrylate) (PMMA) polymer film (Figure 2b). Fitting such spectra with a double-Gaussian profile yields a broad band (named Band-*B*) centered at ~1.60 eV with a fwhm of ~290 meV and a narrower one (named Band-*N*)


https://doi.org/10.1021/acsnano.1c04909
ACS Nano 2021, 15, 17573−17581

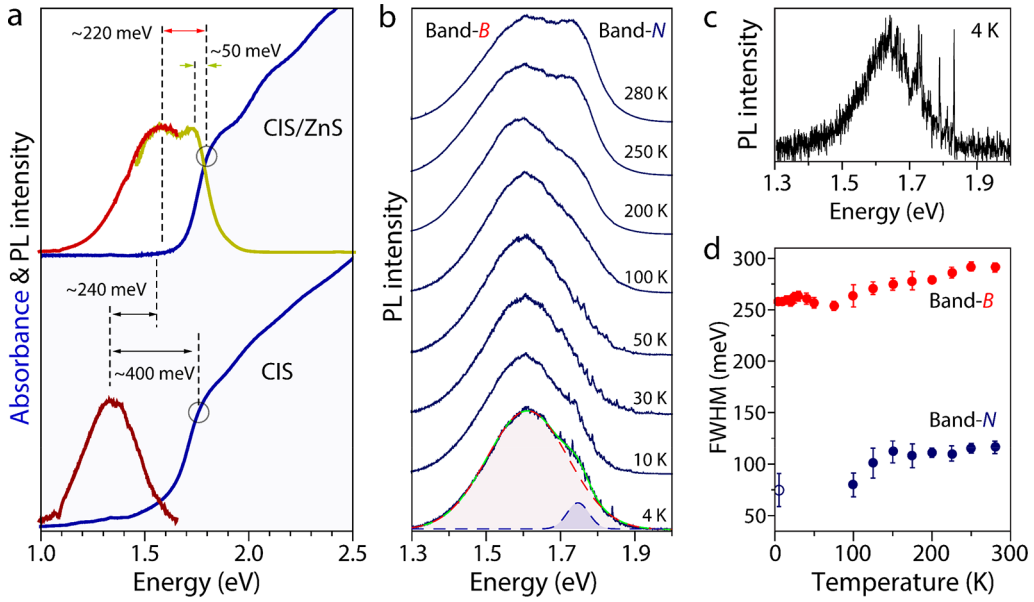


**Figure 2. Ensemble absorption and emission spectra of CIS nanocrystals. (a) Room temperature absorption and PL spectra of wz-CIS QDs suspended in toluene before and after ZnS shelling. As the emission of the CIS/ZnS QDs stands at the edge of the efficiency range of the visible and near-infrared detectors, their PL spectrum was recorded using both visible (yellow line) and near-infrared (red line) detectors. The excitation energy is 2.8 eV. The first absorption peaks ($E_{CIS}$ ~ 1.759 eV; $E_{CIS/ZnS}$ ~ 1.802 eV) marked by hollow circles are located by finding the minima of the second derivative of the absorption spectra (see the SI, Figure S4). (b) Temperature-dependent ensemble PL spectra of the product CIS/ZnS QDs in a PMMA polymer film from 280 to 4 K. The spectrum at 4 K is fitted with a double-Gaussian profile (green line). The fit resolves two bands centered at 1.61 eV (Band-*B*, red dashed profile) and 1.75 eV (Band-*N*, blue dashed profile), respectively. A statistical fine structure is observed in Band-*N* below 100 K. (c) Ensemble PL spectrum of diluted CIS/ZnS QDs at 4 K. Pronounced sharp lines are observed over the Band-*N*. (d) Temperature dependence of the PL line widths of Band-*B* and the Band-*N*. The blue hollow circle gives an estimation of the low-temperature inhomogeneous width of Band-*N*.**

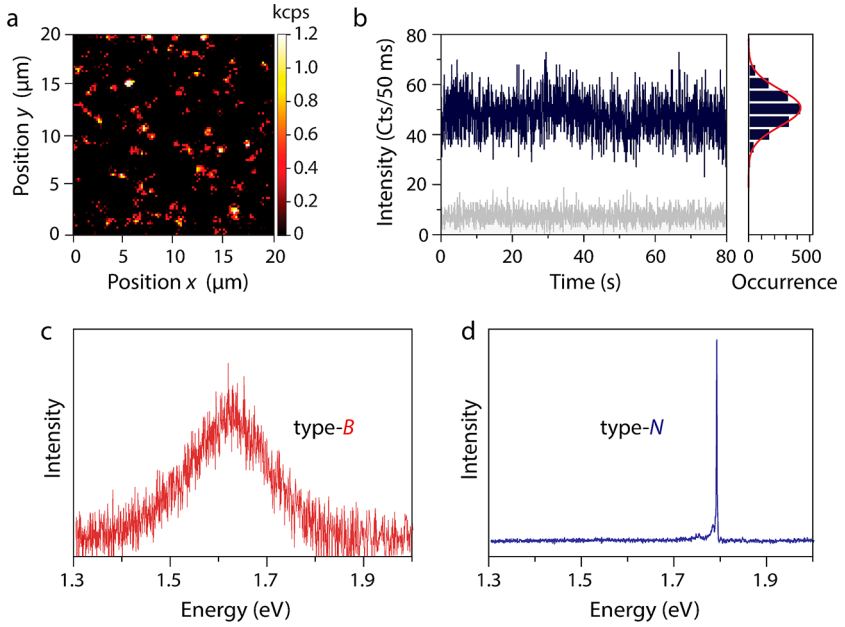


**Figure 3. Spectroscopic features of single wz-CIS/ZnS nanocrystals at 4 K. (a) Confocal PL image of individual wz-CIS/ZnS QDs dispersed in a PMMA film at 4 K, which were excited at 561 nm with a cw intensity of ~2 kW cm$^{-2}$. The color bar indicates the PL intensity. (b) Time trace of the PL intensity of a single QD at 4 K, recorded under the same excitation conditions and with a bin time of 50 ms. The distribution of photon counts per bin is well fit with a Poisson distribution calculated using the mean number of counts (red curve). The gray line is the time trace of the sample PL background. (c and d) PL spectra of representative broad-emitting (c, type-*B*) and narrow-emitting (d, type-*N*) single CIS/ZnS QDs recorded under the same conditions.**

centered at ~1.74 eV with a fwhm of ~110 meV. The relative weights of both bands vary in different regions of the polymer film (SI Figure S5), pointing to nonuniform distributions of two different emitting species that are responsible for these two bands. Band-*B* displays a large Stokes shift (~220 meV) very similar to those observed for both tetragonal cp-CIS[1−5] and



https://doi.org/10.1021/acsnano.1c04909
ACS Nano 2021, 15, 17573−17581

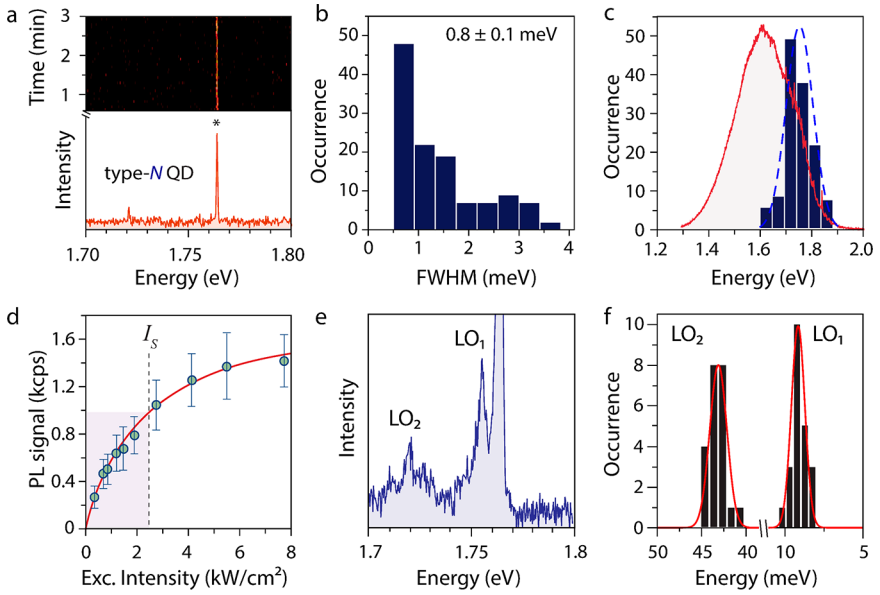


**Figure 4. PL spectra of single type-*N* nanocrystals at 4 K. (a) Spectral trail of a single type-*N* QD (upper panel) built with 36 consecutive spectra recorded with an integration time of 5 s under an excitation intensity of 400 W cm$^{-2}$. The PL spectrum of the bottom panel was obtained by summing all frames of the spectral trail after shifting them to get rid of the spectral diffusion. (b) Histogram of the ZPL widths of more than a hundred type-*N* single QDs. (c) The blue histogram displays their distribution of ZPL energies. It is fit by a Gaussian profile (dashed blue line) with a fwhm ∼100 meV and maps well onto the structured red-wing of the PL ensemble spectrum (red profile). (d) The PL signal (after background subtraction) of a QD is plotted as a function of the excitation intensity. It is fit (red line) with the saturation law $R(I) = R_\infty (I/I_s)/(1+ I/I_s)$, where $R_\infty$ denotes the maximal count rate, $I$ denotes the excitation intensity, and $I_S$ the saturation intensity, which is here 2.4 kW cm$^{-2}$. (e) Zoomed-in PL spectrum of a single QD built over 10 min of integration using the same method as in that in panel a, highlighting the observation of two main longitudinal optical phonon modes named $LO_1$ and $LO_2$. (f) Histograms of the $LO_1$ and $LO_2$ phonon energies centered on 9.2 and 43.2 meV, respectively.**

hexagonal wz-CIS[12,29] QDs. Band-*B* can thus be ascribed to the recombination of delocalized CB electrons and localized Cu-related holes. In contrast, the narrow Band-*N* shows a weak Stokes shift (∼50 meV in Figure 2a) highly comparable to that of the prototypical binary II−VI and III−V QDs.[13,15] Therefore, we attribute Band-*N* to the radiative recombination of the band-edge exciton within the subpopulation of defect-free particles.

When lowering the temperature, Band-*N* loses weight in the ensemble PL spectrum of CIS/ZnS QDs (Figure 2b). Below 100 K, it becomes structured with the onset of many sharp emission lines. At 4 K, the peaks have line widths in the millielectronvolt range and appear more distinctly as the QD concentration decreases (Figure 2c), recalling a regime commonly referred to as "statistical fine structure"[37] (see SI Figure S6). The lines are randomly distributed within an inhomogeneous bandwidth of ∼80 meV and are individually sensitive to photobleaching upon resonant excitation (SI Figure S7), showing evidence that they belong to single particles. In contrast, Band-*B* remains smooth and its line width slightly narrows to ∼260 meV at 4 K (Figure 2d), suggesting that it is dominated by a homogeneous broadening process that persists at liquid helium temperatures.

To gain a deeper insight into the origins of the two bands, single-dot spectroscopy was performed at 4 K. Figure 3a displays a confocal PL image of individual wz-CIS/ZnS QDs dispersed in a PMMA film under a continuous wave (cw) laser excitation at a wavelength of 561 nm. For about half of them, the luminescence is stable with shot-noise-limited intensity fluctuations measured over minutes of acquisition times, as exemplified by the PL time trace of a single QD in Figure 3b (see also SI Figure S8). A systematic investigation of the PL spectra of numerous individual QDs reveals two very distinct classes of emission that do not coexist at the single-particle level. Indeed, single QDs either show a broad line (fwhm ∼210 meV) centered around ∼1.61 eV (Figure 3c) or exhibit an ultranarrow ZPL (fwhm ∼1 meV) at higher energies (Figure 3d). Other examples of PL spectra are presented in SI Figure S9. We infer that the broad-emitting QDs (type-*B*), whose histograms of peak energies and bandwidths are shown in SI Figure S10, contribute to Band-*B* of the ensemble PL spectrum, while the narrow-emitting ones (type-*N*), which account for about 40% of the ensemble of QDs, are likely the origin of Band-*N*.

In the following, we focus on the optical properties of single type-*N* QDs. Figure 4a (upper panel) exemplifies a single-QD PL spectral trail recorded over 3 min at 4 K. Using a weak excitation intensity (∼400 W cm$^{-2}$), the ZPL undergoes reduced spectral diffusion (see more examples in SI Figures S11 and S12). By shifting the spectra along the trail so that the residual ZPL excursions are eliminated and summing all of them, high-quality integrated PL spectra are built (Figure 4a, bottom panel, and SI Figure S13). The distribution of PL line widths of Figure 4b, which were built over more than 120 single QDs, shows that more than 40% of the nanocrystals exhibit sub-millielectronvolt ZPL line widths reaching the resolution limit of the spectrograph (∼0.72 meV). The PL peak energies span from 1.6 to 1.9 eV, and their histogram can be reproduced with a Gaussian profile that closely matches the spectral distribution of Band-*N* in the ensemble PL spectra of Figure 2b. This strengthens the assignment of Band-*N* to type-*N* QDs and therefore the argument that it arises from radiative recombination of the band-edge exciton.



https://doi.org/10.1021/acsnano.1c04909
ACS Nano 2021, 15, 17573−17581

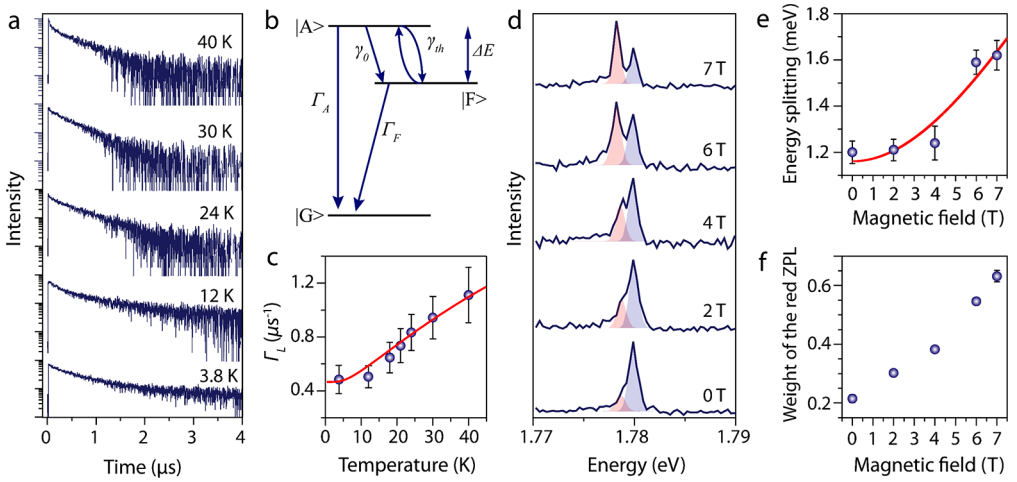


**Figure 5. Band-edge exciton fine structure and relaxation dynamics. (a) Evolution of the PL decay of a single type-*N* wz-CIS/ZnS QD with temperature under pulsed excitation at 561 nm with an average intensity of 75 W cm$^{-2}$. (b) Scheme of the three-level model, where $\Gamma_A$ and $\Gamma_F$ are the radiative relaxation rates of $|A\rangle$ and $|F\rangle$, respectively, $\Delta E$ is the energy splitting between these states, and $\gamma_0$ is the zero-temperature spin-flip rate. The thermal mixing rate $\gamma_{th}$ between $|A\rangle$ and $|F\rangle$ is given by $\gamma_{th} = \gamma_0 N_B$, where $N_B = [\exp(\Delta E/k_B T) - 1]^{-1}$ is the Bose−Einstein acoustic phonon number at temperature $T$. (c) Temperature dependence of the long-component decay rate $\Gamma_L$. The red curve is a fit with $\Gamma_A = 5\ \mu s^{-1}$, $\Gamma_F = 0.46\ \mu s^{-1}$, $\gamma_0 = 0.5\ \mu s^{-1}$, $\Delta E = 1.6$ meV. (d) Evolution of the PL spectrum of a single type-*N* CIS QD under various magnetic field amplitudes at 4 K. It is fit with a double Gaussian profile (blue and red peaks). (e) Energy splitting between the two ZPLs as a function of the magnetic field. The red curve is a fit using the expression of Δ. (f) The weight of the ZPL assigned to $|F\rangle$ increases with the magnetic field. The data in panels e and f and their associated error bars were obtained from the fits in panel d.**

Figure 4d shows the intensity dependence of the emission rate detected for the QD in Figure 4a (other examples are presented in SI Figure S14). After a linear increase at low excitation intensities, a saturation behavior is visible as a clear signature of an efficient nonradiative Auger process.[38,39] Fitting the intensity dependence of the PL signal with the saturation law (Figure 4d) yields the saturation intensity ∼2.4 kW cm$^{-2}$ from which the absorption cross-section is estimated to ∼3.7 × 10$^{-16}$ cm$^2$ for this QD using an exciton lifetime of ∼400 ns. This derivation is fairly consistent with the value of 1.3 × 10$^{-15}$ cm$^2$ extracted from the molar absorption coefficient of a room temperature QD solution (see Supplementary Note 1). Interestingly, the zoomed-in single QD spectrum of Figure 4e reveals two main longitudinal optical phonon sidebands at 9.2 and 43.2 meV (Figure 4f) that match the Raman scattering peaks of wz-CIS nanocrystals (SI Figure S15). Compared with ensemble measurements of CIS QDs where the exciton recombination lines are hidden by inhomogeneous broadening, spectroscopic studies of single QDs allow the determination of phonon contributions to the thermal broadening of the homogeneous line and the exciton relaxation mechanisms. As described in SI Figure S16, the PL spectrum of type-*N* CIS QDs exhibits a continuous redshift with temperature as a consequence of thermal expansion of the lattice and the electron−phonon interaction.[40] From the linear thermal broadening of the ZPL up to 50 K, we deduce an exciton-acoustic phonon coupling coefficient of ∼63 $\mu$eV K$^{-1}$, which is highly comparable to that of the prototypical II−VI QDs.[41−43]

The temperature dependence of the PL decay of a single type-*N* CIS QD is displayed in Figure 5a. At 4 K, the PL decay is biexponential with a fast decay component within a few hundred nanoseconds and a much slower one with a lifetime of $\Gamma_L^{-1}$ in the microsecond range (other examples are presented in SI Figure S17a,b). With increasing temperatures, both components shorten, and the long one gains weight at the expense of the fast one, which vanishes above 50 K. This behavior is the hallmark of the thermal mixing between exciton fine-structure sublevels involving an optically active ("allowed") exciton state named $|A\rangle$ and a low-lying long-lived ("forbidden") one named $|F\rangle$,[44] which is optically inactive with respect to the selection rule on the total exciton angular momentum. The thermalization between these sublevels can be modeled on the basis of a three-level system, including the zero-exciton ground state (Figure 5b). The energy splitting of ∼1.6 meV between $|A\rangle$ and $|F\rangle$ was deduced by fitting the temperature dependence of the long-component PL decay rate $\Gamma_L$ (Figure 5c). Importantly, the lifetime of the bright exciton in CIS QDs was found to be more than one order of magnitude longer than that of CdSe QDs,[44] meaning that the radiative recombination from this state is weakly allowed.

To further reveal the exciton fine structure in CIS nanocrystals, magneto-optical spectroscopy of individual type-*N* CIS QDs was performed, as exemplified in Figure 5d. In zero field, the spectrum is comprised of a dominant ZPL and a weak line in its low-energy wing. When raising the magnetic field, both ZPLs split further apart and the lower-energy one gains weight until it dominates the PL spectrum at 7 T. As observed in individual CdSe QDs,[45,46] this behavior is a signature of the magnetic brightening of a low-lying optically inactive exciton state. Fitting the energy splitting Δ with the expression $\Delta = \sqrt{\Delta_0^2 + (g_\perp^{exc}\mu_B B)^2}$, where $\Delta_0$ is the zero-field splitting, $B$ is the amplitude of the magnetic field nearly perpendicular to the nanocrystal symmetry axis, $\mu_B$ the Bohr magneton, and $g_\perp^{exc}$ is the exciton $g$-factor for a field orthogonal to the crystal axis, yields $\Delta_0 \sim 1.2$ meV, which is comparable to the energy splitting estimated from the temperature evolution of the decay rates. The $g$-factor $g_\perp^{exc} \sim 2.8$ is similar to that measured on single CdSe QDs.[46] The spin-flip rate between the two fine structure sublevels can readily be deduced from the relative weights of the bright and dark ZPLs using the solutions of the rate equations (see SI Figure S18). This rate, which was estimated to 1.4 $\mu s^{-1}$ in zero field, is much lower


https://doi.org/10.1021/acsnano.1c04909
ACS Nano 2021, 15, 17573−17581

than the relaxation rate of the bright exciton in accordance with the observation of the dominant contribution of the |A⟩ exciton ZPL in the PL spectrum. It was found to accelerate with the magnetic field, up to 6 $\mu s^{-1}$ at 7 T, as a result of two possible mechanisms: the increased splitting, which enables a larger density of phonon modes to assist the relaxation,[47] or the admixture in the optically inactive state of |A⟩, which breaks the selection rules inhibiting the |A⟩-to-|F⟩ relaxation.[48]

We have attributed the sharp emission from type-*N* QDs to the radiative recombination of the band-edge exciton. This emission pathway has been put forward in the model of the valence-band fine structure proposed by Shabaev et al.,[26] which predicts that the optical transitions between the electron and hole ground states are weakly allowed for cp-CIS QDs with a spherical shape. Indeed, while the lowest-energy electron and hole levels have respectively *s*-type and *p*-type symmetries, interactions due to the anisotropic crystal structure induce a mixture of odd and even hole states, leading to a radiative recombination of the ground exciton. Additionally, the deviations from spherical shapes measured on our QDs will further promote the mixing of the hole states and therefore foster one-photon optical transition.[49] The observation of narrow ZPLs associated with long-lived exciton fine structure states for type-*N* QDs is a direct signature of this emission pathway. We also attribute the lowest absorption peak at 1.8 eV (Figure 2a) to this band-edge exciton transition (*p*-type hole to *s*-type electron) and thus consider the absence of a Stokes shift in the emission of these QDs. This assignment is at variance with the interpretations of ref 26, where the lowest absorption peak is attributed to the higher-energy symmetry-allowed transition (*s*-type hole to *s*-type electron). The latter transition, which was invoked to explain the large Stokes shifts observed in CIS nanocrystals (such as type-*B* QDs), may actually correspond to the second absorption peak identified at 2.1 eV. Furthermore, the smooth and ultrabroad emission from single type-*B* QDs at liquid helium temperatures cannot be explained by the band-edge hole-level inversion model[26] and is here attributed to the radiative recombination of a delocalized CB electron with a localized hole.

We now discuss the possible mechanisms for the emission of type-*B* QDs, which are characterized by a broad line width and a multiexponential decay (SI Figure S17c and d). The PL broadening could result from multiple randomly located $Cu^+$-related defects producing various energy levels in the gap.[18] In this case, the low-temperature emission line of a QD should display sharp substructures[25] that are inconsistent with the observed large single-QD lines (210 ± 35 meV) with nearly identical peak energies (1.61 ± 0.03 eV), as shown in SI Figure S10. Indeed, assuming a homogeneous substructure contribution of a few millielectronvolts for each defect,[25] such line widths imply that at least 30% of the unit cells would contain Cu defects, which is ruled out given the stoichiometric characterization of the QDs (Figure 1). Thus, our spectroscopic observations suggest that the emission from type-*B* QDs is due to the radiative recombination of a band-edge electron with a self-trapped hole.[16,19,20] However, an intrinsic self-trapping mechanism[16] can be ruled out since it is absent in type-*N* QDs that represent a significant fraction of the QDs in the sample. We infer that the nature of exciton self-trapping in type-*B* QDs should be essentially extrinsic, i.e., defect-assisted.

Defect-assisted self-trapping of charge carriers holds that the combined effects of a weak defect potential and the intrinsic self-induced lattice distortions may produce a localized exciton state.[50] We propose that the spatial positions of defects in the CIS core prior to ZnS shelling determine the fate of the QD emission pathway. For example, due to $Cu^+$ for $Zn^{2+}$ cation exchange,[2,31,33] ZnS shelling is expected to remove most Cu-related defects sitting near the surface of the CIS core, thus preventing the occurrence of an exciton self-trapping process in this region. In such aliovalent cation exchange, the charge balance is preserved through the exchange of different numbers of incoming and outgoing cations with very different solid-state diffusion coefficients (one $Zn^{2+}$ replacing two fast-diffusing $Cu^+$ cations).[51,52] For QDs that do not present hole localization sites deeply embedded in the core, the direct band-edge exciton radiative recombination becomes possible. Such QDs are the *N*-type QDs, while *B*-type ones have hole localization sites in the core that are not affected by ZnS shelling and therefore show broad emission due to extrinsic self-trapping. The recent observation of correlations between reproducible emission energies and lifetimes of single CIS QDs provides evidence that the hole localizes on preferential Cu sites in CIS QDs.[21] Although the nature of these preferred Cu sites remains unclear, our work shows that they may be eliminated or rendered unfavorable for hole localization by ZnS shelling, as evidenced by the type-*N* QDs. The relative increase in the intensity of Band-*N* with respect to that of Band-*B* when increasing the temperature (Figure 2b) can then be explained by the thermal deactivation of the self-trapping process and the promotion of band-edge emission.[53]

## CONCLUSIONS

We have performed low-temperature single quantum dot spectroscopy of core−shell CIS/ZnS nanocrystals and revealed two subpopulations of particles with two distinct exciton relaxation pathways. One class exhibits ultrabroad PL spectra due to extrinsic self-trapping of the hole, which is assisted by defects in imperfectly passivated QDs, while the other shows extremely sharp emission lines attributed to radiative recombination of the band-edge exciton in well-passivated QDs. Spectral and temporal signatures of the two lowest-energy long-lived optically active and inactive excitons are also unveiled under magnetic fields and thermal mixing and give insights into the symmetries of the band-edge hole levels. Further investigation will aim at modeling the exciton fine structure in the view of a potential use in quantum optics and spin-state manipulation. Our spectroscopic study also provides direct evidence of the possibility to produce CIS-based type-*N* QDs with room-temperature line widths comparable to those of the prototypical Cd- or Pb-based QDs. Further developments will consist of implementing chemical strategies to eliminate the defects in the CIS cores and thus improve the fraction of type-*N* QDs. Possible routes will be based on the well-controlled synthesis of high-quality CIS cores, post-treatment by thermal annealing, and fine-tuning of the alloying procedure prior to the overgrowth of shell materials. Another possibility is to explore shelling materials and procedures that prevent the generation of intrabandgap defect levels caused by ion diffusion. These developments would allow the synthesis of narrow-emitting CIS QDs for applications such as light sources, high-color-definition displays, and precise multiplexed sensing and labeling.

## METHODS

**Materials.** We use copper(I) acetate (CuAc, 97%), indium acetate ($In(Ac)_3$, 99.99%), 1-dodecanethiol (DDT, ≥98%), trioctylphosphine



https://doi.org/10.1021/acsnano.1c04909
ACS Nano 2021, 15, 17573−17581

(TOP, 99%), trioctylphosphine oxide (TOPO, 90%), 1-octadecene (ODE, 90%), oleic acid (OA, 90%), zinc stearate ($Zn(St)_2$, technical grade), poly(methyl methacrylate) (PMMA, average $M_w$ of 350 000), indocyanine green (United States Pharmacopeia Reference Standard), anhydrous toluene, methanol, butanol, and dimethyl sulfoxide purchased from Sigma-Aldrich. TOPO, OA, and ODE were separately degassed at 120 °C under vacuum overnight prior to synthesis.

**Synthesis and Characterization of wz-CIS/ZnS QDs.** The wz-CIS/ZnS QDs were synthesized via multiple steps in a standard schlenkline according to previously reported procedures[12] with some modifications. To start, CuAc (1 mmol, 0.126 g), TOPO (4.65 mmol, 1.834 g), and 10 mL of ODE were degassed at 100 °C for 1 h. The turbid solution was purged by $N_2$ and further heated to 210 °C. At 160 °C, 2.5 mL of DDT was swiftly injected into the solution, and the mixture was kept at 210 °C for 30 min before being naturally cooled to room temperature. The crude $Cu_{2-x}S$ nanocrystals were washed twice by repeated precipitation using a mixture of isometric butanol and methanol, centrifuged at 2500 rpm for 15 min, and redispersed in anhydrous toluene. The dark brown $Cu_{2-x}S$ NC precipitates were finally dispersed in 5 mL of DDT and 5 mL of ODE and stored in a glovebox for further use. In the meantime, $In(Ac)_3$ (0.2 mmol, 0.0584 g), TOP (0.2 mmol, 100 $\mu$L), and 2 mL of ODE were mixed and degassed at 125 °C for 1 h. The flask containing the In−TOP complex solution was then refilled with $N_2$ and maintained at 125 °C for the fast injection of the aforementioned 10 mL of the $Cu_{2-x}S$ NCs solution. The mixture was vigorously stirred and kept at 125 °C for 3 h to ensure a complete reaction, then naturally cooled to room temperature. The product CIS QDs were purified twice using the same washing steps described above, then dispersed into 10 mL of DDT, sealed well, and stored in a glovebox for the overgrowth of the ZnS shell.

In a typical ZnS shelling procedure, 2 mL of as-prepared CIS QDs solution and 8 mL of DDT were loaded into a 100 mL three-neck flask. The solution was degassed at 120 °C for 1 h and then purged by $N_2$. At this temperature, a Zn stock solution made of $Zn(St)_2$ (0.3 mmol, 0.1897g) in 1 mL of TOP and 9 mL of ODE was slowly injected into the CIS solution at a rate of 10 mL $h^{-1}$. The mixture was heated to 200 °C and kept at this temperature for 90 min before being cooled to 120 °C. The solution was again degassed for 30 min and then heated to 220 °C under a $N_2$ flow. Once the temperature stabilized at 220 °C, a ZnS stock solution, which was prepared by dissolving 4 mmol $Zn(St)_2$ in 10 mL of OA, 10 mL of DDT, and 20 mL of ODE, was injected into the flask at a rate of 2 mL $h^{-1}$ for 15 h using a syringe pump. Afterward, the solution was annealed for another 3 h before being naturally cooled to 80 °C. The product QDs were purified three times by the same washing procedures mentioned above and finally dispersed in 4 mL of anhydrous toluene.

**Characterization.** Samples for optical characterization (absorption and PL spectra) were prepared by dispersing the product CIS/ZnS QDs into 3 mL of anhydrous toluene in sealable quartz cuvettes under $N_2$. The PL quantum yields were measured using indocyanine green in anhydrous dimethyl sulfoxide as a standard. Powder X-ray diffraction patterns were collected using a Co K$\alpha$ X-ray source at 1.79026 Å. For conventional and high-resolution TEM imaging, electron diffraction, high-angle annular dark field-scanning TEM, and elemental mapping, the samples were diluted, drop-casted on a 200-mesh copper grid, and dried under vacuum for 1 h. The elemental mapping measurements were performed over an acquisition time of 15−20 min with no substantial carbon contamination build-up.

**Low-Temperature Single-Dot Spectroscopy.** For single QD measurements, a dilute solution of CIS/ZnS QDs in toluene was mixed with a 2 wt % solution of PMMA in toluene and then spin-coated onto a clean sapphire coverslip with a rotation speed of 2000 rpm for 100 s. A home-built scanning confocal microscope based on a 0.95 numerical aperture objective was placed in a cryostat and used to image single QDs excited with the 561 nm line of a cw laser. Superconducting coils provided a magnetic field parallel to the objective axis, thus allowing magneto-optical studies in the Faraday configuration. The emitted photons were filtered from the scattered excitation light by a long-pass filter and sent to a single-photon-counting avalanche photodiode and a spectrometer. The PL decay measurements were performed with a conventional time-correlated single-photon-counting setup using a pulsed laser source (optical parametric oscillator at 561 nm, 200 fs pulse width) and a pulse picker to reduce the repetition rate to ∼100 kHz. To obtain the net signal from single QDs, all PL measurements were corrected by subtracting the background.

## ASSOCIATED CONTENT

### Supporting Information

The Supporting Information is available free of charge at https://pubs.acs.org/doi/10.1021/acsnano.1c04909.

Characterization of the QDs, QD absorption spectra, room- and low-temperature PL spectra, example PL spectra and decays of type-*B* and type-*N* CIS/ZnS single QDs at 4 K; PL time traces of a single QD with different excitation intensities, histograms of PL peak intensities and line widths for type-*B* QDs, spectral trail of a single type-*N* QD, effect of prolonged intense laser excitation on single QDs, saturation plots of single type-*N* QDs, estimation of the QD absorption cross section, optical phonon modes, PL spectrum temperature dependence, and arelaxation schemes within the two-level system (PDF)

## AUTHOR INFORMATION


### Corresponding Author

**Brahim Lounis** − *LP2N, Université de Bordeaux, Talence F-33405, France; LP2N, Institut d'Optique and CNRS, Talence F-33405, France;* orcid.org/0000-0001-7501-0236; Email: brahim.lounis@u-bordeaux.fr

### Authors

**Chenghui Xia** − *LP2N, Université de Bordeaux, Talence F-33405, France; LP2N, Institut d'Optique and CNRS, Talence F-33405, France;* orcid.org/0000-0001-5087-8805

**Philippe Tamarat** − *LP2N, Université de Bordeaux, Talence F-33405, France; LP2N, Institut d'Optique and CNRS, Talence F-33405, France*

**Lei Hou** − *LP2N, Université de Bordeaux, Talence F-33405, France; LP2N, Institut d'Optique and CNRS, Talence F-33405, France*

**Serena Busatto** − *Condensed Matter and Interfaces, Debye Institute for Nanomaterials Science, Utrecht University, 3508 TA Utrecht, The Netherlands*

**Johannes D. Meeldijk** − *Electron Microscopy Utrecht, Debye Institute for Nanomaterials Science, Utrecht University, 3584 CH Utrecht, Netherlands*

**Celso de Mello Donega** − *Condensed Matter and Interfaces, Debye Institute for Nanomaterials Science, Utrecht University, 3508 TA Utrecht, The Netherlands;* orcid.org/0000-0002-4403-3627

Complete contact information is available at: https://pubs.acs.org/10.1021/acsnano.1c04909


### Notes

The authors declare no competing financial interest.

## ACKNOWLEDGMENTS

We warmly thank Alexander Efros for fruitful discussions and comments. C.X. acknowledges the group of Condensed Matter and Interfaces, Utrecht University for providing a platform for

doing chemical synthesis and structural characterizations. We acknowledge the financial support from the French National Agency for Research, Région Aquitaine, Institut Universitaire de France, Idex Bordeaux (GPR LIGHT), and the EUR Light S&T.

## REFERENCES

(1) Knowles, K. E.; Hartstein, K. H.; Kilburn, T. B.; Marchioro, A.; Nelson, H. D.; Whitham, P. J.; Gamelin, D. R. Luminescent Colloidal Semiconductor Nanocrystals Containing Copper: Synthesis, Photophysics, and Applications. *Chem. Rev.* **2016**, *116*, 10820−10851.

(2) Berends, A. C.; Mangnus, M. J. J.; Xia, C.; Rabouw, F. T.; de Mello Donega, C. Optoelectronic Properties of Ternary I−III−$VI_2$ Semiconductor Nanocrystals: Bright Prospects with Elusive Origins. *J. Phys. Chem. Lett.* **2019**, *10*, 1600−1616.

(3) Leach, A. D. P.; Macdonald, J. E. Optoelectronic Properties of $CuInS_2$ Nanocrystals and Their Origin. *J. Phys. Chem. Lett.* **2016**, *7*, 572−583.

(4) Moodelly, D.; Kowalik, P.; Bujak, P.; Pron, A.; Reiss, P. Synthesis, Photophysical Properties and Surface Chemistry of Chalcopyrite-Type Semiconductor Nanocrystals. *J. Mater. Chem. C* **2019**, *7*, 11665−11709.

(5) Long, Z.; Zhang, W.; Tian, J.; Chen, G.; Liu, Y.; Liu, R. Recent Research on the Luminous Mechanism, Synthetic Strategies, and Applications of $CuInS_2$ Quantum Dots. *Inorg. Chem. Front.* **2021**, *8*, 880−897.

(6) Rao, H.; Zhou, M.; Pan, Z.; Zhong, X. Quantum Dot Materials Engineering Boosting the Quantum Dot Sensitized Solar Cell Efficiency over 13%. *J. Mater. Chem. A* **2020**, *8*, 10233−10241.

(7) Meinardi, F.; McDaniel, H.; Carulli, F.; Colombo, A.; Velizhanin, K. A.; Makarov, N. S.; Simonutti, R.; Klimov, V. I.; Brovelli, S. Highly Efficient Large-Area Colourless Luminescent Solar Concentrators Using Heavy-Metal-Free Colloidal Quantum Dots. *Nat. Nanotechnol.* **2015**, *10*, 878−885.

(8) Anand, A.; Zaffalon, M. L.; Gariano, G.; Camellini, A.; Gandini, M.; Brescia, R.; Capitani, C.; Bruni, F.; Pinchetti, V.; Zavelani-Rossi, M.; Meinardi, F.; Crooker, S. A.; Brovelli, S. Evidence for the Band-Edge Exciton of $CuInS_2$ Nanocrystals Enables Record Efficient Large-Area Luminescent Solar Concentrators. *Adv. Funct. Mater.* **2020**, *30*, 1906629.

(9) Lv, G.; Guo, W.; Zhang, W.; Zhang, T.; Li, S.; Chen, S.; Eltahan, A. S.; Wang, D.; Wang, Y.; Zhang, J.; Wang, P. C.; Chang, J.; Liang, X.-J. Near-Infrared Emission CuInS/ZnS Quantum Dots: All-in-One Theranostic Nanomedicines with Intrinsic Fluorescence/Photoacoustic Imaging for Tumor Phototherapy. *ACS Nano* **2016**, *10*, 9637−9645.

(10) Li, L.; Daou, T. J.; Texier, I.; Kim Chi, T. T.; Liem, N. Q.; Reiss, P. Highly Luminescent $CuInS_2$/ZnS Core/Shell Nanocrystals: Cadmium-Free Quantum Dots for *in Vivo* Imaging. *Chem. Mater.* **2009**, *21*, 2422−2429.

(11) Li, L.; Pandey, A.; Werder, D. J.; Khanal, B. P.; Pietryga, J. M.; Klimov, V. I. Efficient Synthesis of Highly Luminescent Copper Indium Sulfide-Based Core/Shell Nanocrystals with Surprisingly Long-Lived Emission. *J. Am. Chem. Soc.* **2011**, *133*, 1176−1179.

(12) Xia, C.; Meeldijk, J. D.; Gerritsen, H. C.; de Mello Donegá, C. Highly Luminescent Water-Dispersible NIR-Emitting Wurtzite $CuInS_2$/ZnS Core/Shell Colloidal Quantum Dots. *Chem. Mater.* **2017**, *29*, 4940−4951.

(13) Chen, O.; Zhao, J.; Chauhan, V. P.; Cui, J.; Wong, C.; Harris, D. K.; Wei, H.; Han, H. S.; Fukumura, D.; Jain, R. K.; Bawendi, M. G. Compact High-Quality CdSe−CdS Core−Shell Nanocrystals with Narrow Emission Linewidths and Suppressed Blinking. *Nat. Mater.* **2013**, *12*, 445−451.

(14) Cui, J.; Beyler, A. P.; Marshall, L. F.; Chen, O.; Harris, D. K.; Wanger, D. D.; Brokmann, X.; Bawendi, M. G. Direct Probe of Spectral Inhomogeneity Reveals Synthetic Tunability of Single-Nanocrystal Spectral Linewidths. *Nat. Chem.* **2013**, *5*, 602−606.

(15) Won, Y.-H.; Cho, O.; Kim, T.; Chung, D.-Y.; Kim, T.; Chung, H.; Jang, H.; Lee, J.; Kim, D.; Jang, E. Highly Efficient and Stable InP/ZnSe/ZnS Quantum Dot Light-Emitting Diodes. *Nature* **2019**, *575*, 634−638.

(16) Knowles, K. E.; Nelson, H. D.; Kilburn, T. B.; Gamelin, D. R. Singlet−Triplet Splittings in the Luminescent Excited States of Colloidal $Cu^+$:CdSe, $Cu^+$:InP, and $CuInS_2$ Nanocrystals: Charge-Transfer Configurations and Self-Trapped Excitons. *J. Am. Chem. Soc.* **2015**, *137*, 13138−13147.

(17) Whitham, P. J.; Marchioro, A.; Knowles, K. E.; Kilburn, T. B.; Reid, P. J.; Gamelin, D. R. Single-Particle Photoluminescence Spectra, Blinking, and Delayed Luminescence of Colloidal $CuInS_2$ Nanocrystals. *J. Phys. Chem. C* **2016**, *120*, 17136−17142.

(18) Zang, H.; Li, H.; Makarov, N. S.; Velizhanin, K. A.; Wu, K.; Park, Y.-S.; Klimov, V. I. Thick-Shell $CuInS_2$/ZnS Quantum Dots with Suppressed "Blinking" and Narrow Single-Particle Emission Line Widths. *Nano Lett.* **2017**, *17*, 1787−1795.

(19) Nelson, H. D.; Gamelin, D. R. Valence-Band Electronic Structures of $Cu^+$-Doped ZnS, Alloyed Cu−In−Zn−S, and Ternary $CuInS_2$ Nanocrystals: A Unified Description of Photoluminescence across Compositions. *J. Phys. Chem. C* **2018**, *122*, 18124−18133.

(20) Hughes, K. E.; Ostheller, S. R.; Nelson, H. D.; Gamelin, D. R. Copper's Role in the Photoluminescence of $Ag_{1-x}Cu_xInS_2$ Nanocrystals, from Copper-Doped $AgInS_2$ ($x \sim 0$) to $CuInS_2$ ($x = 1$). *Nano Lett.* **2019**, *19*, 1318−1325.

(21) Hinterding, S. O. M.; Mangnus, M. J. J.; Prins, P. T.; Jöbsis, H. J.; Busatto, S.; Vanmaekelbergh, D.; de Mello Donega, C.; Rabouw, F. T. Unusual Spectral Diffusion of Single $CuInS_2$ Quantum Dots Sheds Light on the Mechanism of Radiative Decay. *Nano Lett.* **2021**, *21*, 658−665.

(22) Fuhr, A.; Yun, H. J.; Crooker, S. A.; Klimov, V. I. Spectroscopic and Magneto-Optical Signatures of $Cu^{1+}$ and $Cu^{2+}$ Defects in Copper Indium Sulfide Quantum Dots. *ACS Nano* **2020**, *14*, 2212−2223.

(23) Vale, B. R. C.; Socie, E.; Cunha, L. R. C.; Fonseca, A. F. V.; Vaz, R.; Bettini, J.; Moser, J.-E.; Schiavon, M. A. Revealing Exciton and Metal−Ligand Conduction Band Charge Transfer Absorption Spectra in Cu-Zn-In-S Nanocrystals. *J. Phys. Chem. C* **2020**, *124*, 27858−27866.

(24) van der Stam, W.; de Graaf, M.; Gudjonsdottir, S.; Geuchies, J. J.; Dijkema, J. J.; Kirkwood, N.; Evers, W. H.; Longo, A.; Houtepen, A. J. Tuning and Probing the Distribution of $Cu^+$ and $Cu^{2+}$ Trap States Responsible for Broad-Band Photoluminescence in $CuInS_2$ Nanocrystals. *ACS Nano* **2018**, *12*, 11244−11253.

(25) Binsma, J. J. M.; Giling, L. J.; Bloem, J. Luminescence of $CuInS_2$: II. Exciton and Near Edge Emission. *J. Lumin.* **1982**, *27*, 55−72.

(26) Shabaev, A.; Mehl, M. J.; Efros, A. L. Energy Band Structure of $CuInS_2$ and Optical Spectra of $CuInS_2$ Nanocrystals. *Phys. Rev. B: Condens. Matter Mater. Phys.* **2015**, *92*, 035431.

(27) Pons, T.; Pic, E.; Lequeux, N.; Cassette, E.; Bezdetnaya, L.; Guillemin, F.; Marchal, F.; Dubertret, B. Cadmium-Free $CuInS_2$/ZnS Quantum Dots for Sentinel Lymph Node Imaging with Reduced Toxicity. *ACS Nano* **2010**, *4*, 2531−2538.

(28) Tomić, S.; Bernasconi, L.; Searle, B. G.; Harrison, N. M. Electronic and Optical Structure of Wurtzite $CuInS_2$. *J. Phys. Chem. C* **2014**, *118*, 14478−14484.

(29) Xia, C.; Wu, W.; Yu, T.; Xie, X.; van Oversteeg, C.; Gerritsen, H. C.; de Mello Donega, C. Size-Dependent Band-Gap and Molar Absorption Coefficients of Colloidal $CuInS_2$ Quantum Dots. *ACS Nano* **2018**, *12*, 8350−8361.

(30) Jara, D. H.; Stamplecoskie, K. G.; Kamat, P. V. Two Distinct Transitions in $Cu_xInS_2$ Quantum Dots. Bandgap *versus* Sub-Bandgap Excitations in Copper-Deficient Structures. *J. Phys. Chem. Lett.* **2016**, *7*, 1452−1459.

(31) De Trizio, L.; Prato, M.; Genovese, A.; Casu, A.; Povia, M.; Simonutti, R.; Alcocer, M. J. P.; D'Andrea, C.; Tassone, F.; Manna, L. Strongly Fluorescent Quaternary Cu−In−Zn−S Nanocrystals Prepared from $Cu_{1-x}InS_2$ Nanocrystals by Partial Cation Exchange. *Chem. Mater.* **2012**, *24*, 2400−2406.



https://doi.org/10.1021/acsnano.1c04909
*ACS Nano* 2021, 15, 17573−17581

(32) Xia, C.; Winckelmans, N.; Prins, P. T.; Bals, S.; Gerritsen, H. C.; de Mello Donegá, C. Near-Infrared-Emitting $CuInS_2$/ZnS Dot-in-Rod Colloidal Heteronanorods by Seeded Growth. *J. Am. Chem. Soc.* **2018**, *140*, 5755−5763.
(33) Park, J.; Kim, S.-W. $CuInS_2$/ZnS Core/Shell Quantum Dots by Cation Exchange and Their Blue-Shifted Photoluminescence. *J. Mater. Chem.* **2011**, *21*, 3745−3750.
(34) Tschirner, N.; Lange, H.; Schliwa, A.; Biermann, A.; Thomsen, C.; Lambert, K.; Gomes, R.; Hens, Z. Interfacial Alloying in CdSe/CdS Heteronanocrystals: A Raman Spectroscopy Analysis. *Chem. Mater.* **2012**, *24*, 311−318.
(35) Seo, J.; Raut, S.; Abdel-Fattah, M.; Rice, Q.; Tabibi, B.; Rich, R.; Fudala, R.; Gryczynski, I.; Gryczynski, Z.; Kim, W. J.; Jung, S.; Hyun, R. Time-Resolved and Temperature-Dependent Photoluminescence of Ternary and Quaternary Nanocrystals of $CuInS_2$ with ZnS Capping and Cation Exchange. *J. Appl. Phys.* **2013**, *114*, 094310.
(36) Bose, R.; Ahmed, G. H.; Alarousu, E.; Parida, M. R.; Abdelhady, A. L.; Bakr, O. M.; Mohammed, O. F. Direct Femtosecond Observation of Charge Carrier Recombination in Ternary Semiconductor Nanocrystals: The Effect of Composition and Shelling. *J. Phys. Chem. C* **2015**, *119*, 3439−3446.
(37) Moerner, W. E.; Carter, T. P. Statistical Fine Structure of Inhomogeneously Broadened Absorption Lines. *Phys. Rev. Lett.* **1987**, *59*, 2705−2708.
(38) Klimov, V. I.; Mikhailovsky, A. A.; McBranch, D. W.; Leatherdale, C. A.; Bawendi, M. G. Quantization of Multiparticle Auger Rates in Semiconductor Quantum Dots. *Science* **2000**, *287*, 1011−1013.
(39) Efros, A. L.; Nesbitt, D. J. Origin and Control of Blinking in Quantum Dots. *Nat. Nanotechnol.* **2016**, *11*, 661−671.
(40) Varshni, Y. P. Temperature Dependence of the Energy Gap in Semiconductors. *Physica* **1967**, *34*, 149−154.
(41) Valerini, D.; Cretí, A.; Lomascolo, M.; Manna, L.; Cingolani, R.; Anni, M. Temperature Dependence of the Photoluminescence Properties of Colloidal CdSe/ZnS Core/Shell Quantum Dots Embedded in a Polystyrene Matrix. *Phys. Rev. B: Condens. Matter Mater. Phys.* **2005**, *71*, 235409.
(42) Gaponenko, M. S.; Lutich, A. A.; Tolstik, N. A.; Onushchenko, A. A.; Malyarevich, A. M.; Petrov, E. P.; Yumashev, K. V. Temperature-Dependent Photoluminescence of PbS Quantum Dots in Glass: Evidence of Exciton State Splitting and Carrier Trapping. *Phys. Rev. B: Condens. Matter Mater. Phys.* **2010**, *82*, 125320.
(43) Narayanaswamy, A.; Feiner, L. F.; Meijerink, A.; van der Zaag, P. J. The Effect of Temperature and Dot Size on the Spectral Properties of Colloidal InP/ZnS Core−Shell Quantum Dots. *ACS Nano* **2009**, *3*, 2539−2546.
(44) Biadala, L.; Louyer, Y.; Tamarat, P.; Lounis, B. Direct Observation of the Two Lowest Exciton Zero-Phonon Lines in Single CdSe/ZnS Nanocrystals. *Phys. Rev. Lett.* **2009**, *103*, 037404.
(45) Louyer, Y.; Biadala, L.; Trebbia, J. B.; Fernée, M. J.; Tamarat, P.; Lounis, B. Efficient Biexciton Emission in Elongated CdSe/ZnS Nanocrystals. *Nano Lett.* **2011**, *11*, 4370−4375.
(46) Biadala, L.; Louyer, Y.; Tamarat, P.; Lounis, B. Band-Edge Exciton Fine Structure of Single CdSe/ZnS Nanocrystals in External Magnetic Fields. *Phys. Rev. Lett.* **2010**, *105*, 157402.
(47) Fernée, M. J.; Sinito, C.; Louyer, Y.; Potzner, C.; Nguyen, T.-L.; Mulvaney, P.; Tamarat, P.; Lounis, B. Magneto-Optical Properties of Trions in Non-Blinking Charged Nanocrystals Reveal an Acoustic Phonon Bottleneck. *Nat. Commun.* **2012**, *3*, 1287.
(48) Gandil, M.; Matsuda, K.; Lounis, B.; Tamarat, P. Spectroscopic Signatures of Spin-Orbit Coupling and Free Excitons in Individual Suspended Carbon Nanotubes. *Phys. Rev. B: Condens. Matter Mater. Phys.* **2019**, *100*, 081411.
(49) Nagamine, G.; Nunciaroni, H. B.; McDaniel, H.; Efros, A. L.; de Brito Cruz, C. H.; Padilha, L. A. Evidence of Band-Edge Hole Levels Inversion in Spherical $CuInS_2$ Quantum Dots. *Nano Lett.* **2018**, *18*, 6353−6359.
(50) Song, K. S.; Williams, R. T. *Self-Trapped Excitons*; Springer-Verlag Berlin Heidelberg: Berlin, Germany, 1996; p 410.
(51) Berends, A. C.; van der Stam, W.; Hofmann, J. P.; Bladt, E.; Meeldijk, J. D.; Bals, S.; de Mello Donega, C. Interplay between Surface Chemistry, Precursor Reactivity, and Temperature Determines Outcome of ZnS Shelling Reactions on $CuInS_2$ Nanocrystals. *Chem. Mater.* **2018**, *30*, 2400−2413.
(52) De Trizio, L.; Manna, L. Forging Colloidal Nanostructures *via* Cation Exchange Reactions. *Chem. Rev.* **2016**, *116*, 10852−10887.
(53) Lee, D.; Mysyrowicz, A.; Nurmikko, A. V.; Fitzpatrick, B. J. Exciton Self-Trapping in ZnSe-ZnTe Alloys. *Phys. Rev. Lett.* **1987**, *58*, 1475−1478.


https://doi.org/10.1021/acsnano.1c04909
*ACS Nano* 2021, 15, 17573−17581